



Structural and electrocatalytic properties of molten core Sn@SnO_x nanoparticles on ceria



Luca Bardini^{a,*}, Alfonsina Pappacena^a, Montserrat Dominguez-Escalante^b, Jordi Llorca^b, Marta Boaro^{a,*}, Alessandro Trovarelli^a

^a Dipartimento Politecnico di Ingegneria e Architettura, Università di Udine, via Cotonificio 108, 33100 Udine, Italy

^b Institut de Tècniques Energètiques and Centre for Research in Nanoengineering, Universitat Politècnica de Catalunya, 08028 Barcelona, Spain

ARTICLE INFO

Article history:

Received 27 November 2015

Received in revised form 4 February 2016

Accepted 24 February 2016

Available online 26 February 2016

Keywords:

Ceria

Tin oxide

SOFC

Molten tin

Core-shell

ABSTRACT

The morphological and chemical modifications following reduction in hydrogen at 873 K of stannic oxide deposited on ceria particles were studied in order to gain insights into the nature of Ce-Sn interaction under reducing atmosphere, simulating the operating conditions in a solid oxide fuel cell. It is shown that the co-presence of the two materials improves the power output of fuel cells up to a factor of 10 when compared to ceria alone. Through high resolution transmission electron microscopy (HRTEM), X-ray photoelectron spectroscopy (XPS), and in-situ X-ray diffraction (XRD) data we show the formation of a novel system made up of nanoparticles composed of a molten Sn⁰ core capped by an amorphous tin oxide layer. SnO_x shell acts as a binding agent which stabilizes Sn⁰ nanoparticles on ceria even after reductive treatment at temperatures well above the melting point of tin. This occurs through an interfacial redox communication between ceria and tin, likely involving a transfer of oxygen from ceria to the metal and electrons from metal to ceria. It is highlighted how the Sn@SnO_x nanostructures and their spontaneous formation could be used as a model for the development of catalyst nano-assembly comprising an amorphous metal oxide triple phase boundary, opening the way for a new paradigm in the development of multifunctional catalytic systems.

© 2016 Elsevier B.V. All rights reserved.

1. Introduction

Cerium and Tin based oxides have been studied for their electronic, magnetic, optical and catalytic properties. The main characteristic of ceria is its fast and reversible reducibility that can be finely tuned and controlled by doping or by interacting with metal catalysts [1]; tin oxide is a semiconductor material having a high electrical conductivity, optical transparency and redox properties [2]. The former has been mainly utilized in the field of environmental catalysis [3,4] and fuel cell technology [5,6] while SnO₂ has found application especially as a solid state gas sensor material [7], oxidation catalyst [8] and transparent conductor [9]. When used in combination these oxides generally show an enhancement of their properties that is strongly correlated with their composition and structural/morphological characteristics. The majority of studies on Ce-Sn-O system have been focused on the properties and preparation of M_xCe_{1-x}O_{1-y} (with x = 1 – 0.1,

M = Sn⁴⁺) mixed oxides in forms of powders or films that were investigated in terms of their structural, morphological, electrical and redox characteristics [10–18]. It resulted that CeO₂ contributes to improve surface and bulk oxygen exchange and thermal stability of tin oxide, thus increasing its sensing and catalytic properties. Pivotal for the enhancement of catalytic performances of these binary oxides is the formation of solid solutions [11,16,18,19]; this depends on several factors (i.e. the type of synthesis, the molar ratio between the oxides, the temperature and atmosphere of calcination), and leads to a material with higher oxygen storage capacity. Only a few studies investigated the Ce-Sn interaction in terms of metal-support interface. In this case, DFT calculations [20] and photospectroscopic analysis [21–23] have demonstrated that the deposition of metallic tin on ceria led to the formation of a homogeneous bulk Ce-Sn-O mixed oxide through a non-activated process that involves electrons transfer from the Sn ad-atoms to the substrate, causing the reduction of cerium ions from Ce⁴⁺ to Ce³⁺. This synergism was proposed to be responsible for the higher catalytic activity of the SnO_x/CeO_x mixed oxide catalysts when compared with the individual pure oxides. The potential interest in the use of Ce-Sn-O systems for novel applications in the field of renewable

* Corresponding authors.

E-mail address: marta.boaro@uniud.it (M. Boaro).

energy such as solid electrolyte fuel cells (SOFCs) and solar cells [24] prompted us to investigate in more detail the characteristics of interaction between ceria and tin oxide in view of the above applications.

In recent years cerium oxide has gathered a considerable attention for the development of solid oxide fuel cells (SOFCs) capable to operate at intermediate temperature (873 K or below). Decreasing the working temperature of these systems allows to relax material requirements making SOFCs technology more economically viable. In this regard, ceria has good ionic conductivity and good oxygen storage capacity at temperatures as low as 600 °C [4]. However, its catalytic activity and electronic conductivity need to be further improved. To achieve this goal it is possible to tailor the nanostructure of ceria particles or, alternatively, to add a metal catalyst. Several studies have been pursued to understand the influence of various variables on the catalytic and electronic properties of cerium oxide e.g. the nanostructure/shape of ceria particles [25–30], the size of ceria particles [31], the incorporation of a catalyst inside ceria particles [32], the bonding of a metal to defects on ceria [33–35] as well as oxygen transfer from ceria to a nearby metal [36–39].

Concerning the use of tin oxide in the realm of fuel cells, recent work has focused on tin as an aid to reduce carbon deposition in anodes containing nickel with conflicting results [40–42] and on molten tin anodes at high temperature for use in direct carbon fuel cells [43,44]. Conversely, its use as co-catalyst of ceria has not been investigated yet.

In this work the redox interaction between tin oxide and ceria is studied in SOFC anodes in dry hydrogen at intermediate temperature. It is shown, for the first time, that tin oxide on ceria is reduced to form electro-catalytically active molten metal nanoparticles capped by a thin amorphous oxide shell. These nanoparticles increase the SOFC power output by a factor of 10 when compared to cells infiltrated with ceria alone. The combined use of XRD, HRTEM and XPS analysis revealed that when stannic oxide is deposited on CeO₂, hydrogen induces formation of a new ceria-tin system which comprises molten metallic tin–tin oxide composite nanoparticles stabilized by ceria. The mechanism of formation and the parameters contributing to stabilize the system were discussed with the aim to individuate a new paradigm for the development of metal-support systems based on nano-sized molten metal catalysts. It is highlighted how the amorphous oxidic shell likely plays a prominent role in the oxidation reaction, and how the Sn@SnO_x nanostructures and their spontaneous formation could be used as a model for the development of new nano-catalysts comprising an amorphous metal oxide triple phase boundary.

2. Experimental

2.1. Materials

Button fuel cells 12 mm in diameter were prepared by uni-axially pressing 600 mg of commercial samaria-doped ceria (Ce_{0.8}Sm_{0.2}O_{1.9} Nextech, FuelCell Materials; SDC) for the electrolyte and 150 mg of SDC mixed with 30% w/w commercial starch (Mantovani) as the pore former for the anode. The semi-cell obtained was sintered in air at 1673 K for 3 h with a heating rate of 2 K min^{−1} and cooled at a rate of 5 K min^{−1}. The cathode was a commercial mixture of Lanthanum Strontium Cobalt Ferrite and Gadolinium doped Ceria (50 wt% (La_{0.6}Sr_{0.4})_{0.95}Co_{0.2}OFe_{0.8}O_{3−x}/50 wt% Ce_{0.9}Gd_{0.1}O_{2−x}, Nextech, Fuel Cell Materials, LSCF/GDC) and was applied by painting with 5% w/w vulcan carbon as the pore former, sintered at 1473 K for 3 h with a heating rate of 2 K min^{−1} and cooled in air at 5 K min^{−1}. The anode was then infiltrated with a solution of Ce(NO₃)₃ (Treibacher Industrie AG) and SnCl₂ (Carlo Erba) to

Table 1

Amount of ceria and tin oxide infiltrated in the cells used in the experiments.

	Ceria (Weight%)	Tin (Weight%)	Ce:Sn (molar ratio)
Cell A	20	0	–
Cell B	0	12	–
Cell C	20	6	3
Cell D	20	12	1.5

obtain anodes loaded with ceria and tin respectively. For anodes containing both components, ceria was infiltrated and calcined in air at 873 K before addition of tin. A gold contact was applied on the anode with gold paste, while a silver mesh was applied on the cathode with silver paste.

For HR-TEM and XRD experiments, CeO₂ was prepared by precipitation from commercial cerium(III) nitrate (Treibacher AG). Surface area measured by BET was 25 m² g^{−1}. Ceria was then impregnated with a saturated stannous chloride (Carlo Erba) ethanol solution up to obtain the same Ce/Sn ratio used in the cell D (37.5 w/w%) and calcined in air at 1073 K for 3 h with a heating rate of 10 K min^{−1}. XPS experiments were performed on ceria and tin dispersed in samaria-doped ceria (SDC) pellets. This choice stems from experimental constraints related to the geometry of the XPS gas treatment chamber: a porous supporting matrix, in fact, allowed for a more uniform exposure to hydrogen. We adopted the same matrix and microstructure used for the anode. The SDC scaffolds were prepared from commercial SDC powders (Nextech, FuelCell Materials) mixed with commercial starch (Mantovani) as a pore former. Pellets were then prepared by applying a uniform weight of 500 kg for 1 min and fired in air at 1673 K for 3 h. The porosity of the pellets was measured by Archimedes's technique. 20 mg of CeO₂ were infiltrated in the pellets starting from an aqueous 1.5 M solution of cerium(III) nitrate (Treibacher AG) to reach a CeO₂ loading of 20% w/w. Five successive infiltrations were required, each followed by calcination in air at 873 K for 1 h with a heating rate of 20 K min^{−1}. 12 mg of tin oxide were then infiltrated in the pellets by way of a saturated stannous chloride (Carlo Erba) ethanol solution. Each infiltration step was followed by calcination in air at 673 K for 1 h with a heating rate of 20 K min^{−1} (see Table 1). Finally the pellet was calcined in air at 1073 K for 3 h with a heating rate of 10 K min^{−1}.

2.2. Characterization

All electrochemical experiments were run with an AMEL 7050 potentiostat and an AMEL 7200 frequency response analyzer. Electrochemical impedance (EIS) measurements were conducted in the frequency range 1 MHz–100 mHz with a signal amplitude of 30 mV at the open circuit voltage (OCV). Impedance spectra were analyzed with the Elchemea Analytical 1.3 and ZView software packages. Testing was performed in dry hydrogen at 50 ml min^{−1} since preliminary tests have demonstrated that the performance of the cells are only marginally affected by the gas humidification. A scheme of the setup employed is provided in the supporting information (see ESI, Fig. S1). The reproducibility was checked testing two or three cells for each composition.

Scanning electron microscopy (SEM) images were recorded using an EVO40 microscope operating at an emission voltage of 20 KeV. High resolution transmission electron microscopy studies were performed with a JEOL JEM 2010F electron microscope equipped with a field emission gun working at an accelerating voltage of 200 kV.

In-house X-ray photoelectron spectroscopy (XPS) spectra were collected with a SPECS system equipped with an Al anode XR50 source operating at 150 W and a Phoibos 150 MCD –9 detector. Spectra were recorded with pass energy of 25 eV at 0.1 eV steps at

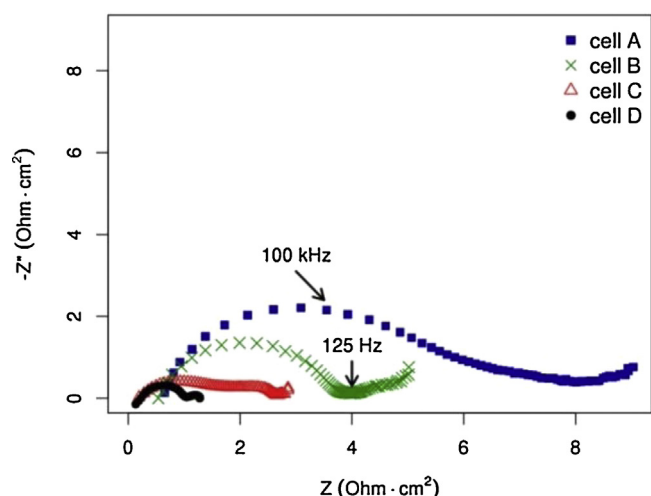


Fig. 1. Nyquist plots in dry hydrogen at 873 K for (□) cell A, (×) cell B, (Δ) cell C and (○) cell D.

a pressure below 5×10^{-12} bar. Binding energies were referred to the adventitious C 1s signal at 285.3 eV.

XRD spectra were recorded using a Philips X'Pert diffractometer equipped with a real time multiple strip detector operated at 40 kV and 40 mA using nickel-filtered Cu K α radiation and an Anton Paar hot chamber. The temperature was increased from 298 K at a heating rate of 10 K min^{-1} stopping at 423 K and 523 K and then lowered back to 298 K. Two XRD spectra were recorded at every isothermal step. Spectra were collected using a step size of 0.02° and a counting time of 40 s per angular abscissa in the range $20\text{--}60$ 2θ degrees. The Philips X'Pert High Score software was used for phase identification.

2.3. Morphological characterization of cells

The compositions studied are presented in Table 1, and include anodes infiltrated with ceria (cell A), tin (cell B), and ceria:tin with molar ratios of 3 (cell C) and 1.5 (cell D). The electrolyte is dense and $380 \mu\text{m}$ thick, while the SDC anode and the cathode have a thickness of $150 \mu\text{m}$ and $20 \mu\text{m}$ respectively. Porosity measured via Archimedes's technique for the anodes is ca. 40%, which is low when compared to other examples [45,46]. Trying to increase the porosity by changing the pore former/SDC ratio resulted in poor adhesion of the anode to the electrolyte, which eventually led to delamination. SEM images also show that the porosity might not be evenly distributed (see ESI, Fig. S2); the surface of the anode, in fact, has wide pore-less areas. Pore size shows a considerable variance, as can be seen in cross section images. These faults are attributable to limitations in the pressing procedure. All these factors are an *a priori* limiting factor for the absolute performance of the cells [45]. It must be noted that these problems were systematic and affected all cells in equal measure.

3. Results and discussion

3.1. Electrochemical testing

Electrochemical tests were conducted at 873 K with pure dry hydrogen fluxed at 50 ml min^{-1} over the anode, while the cathode was exposed to ambient air. The impedance of the cathode was negligible in all experiments. This fact can be attributed to the relatively large impedance generated by the imperfect microstructure of the anode, which overwhelms cathodic contributions. The impedance spectra in Fig. 1 shows how cells infiltrated with tin alone (cell B) generates a polarization resistance significantly lower with respect

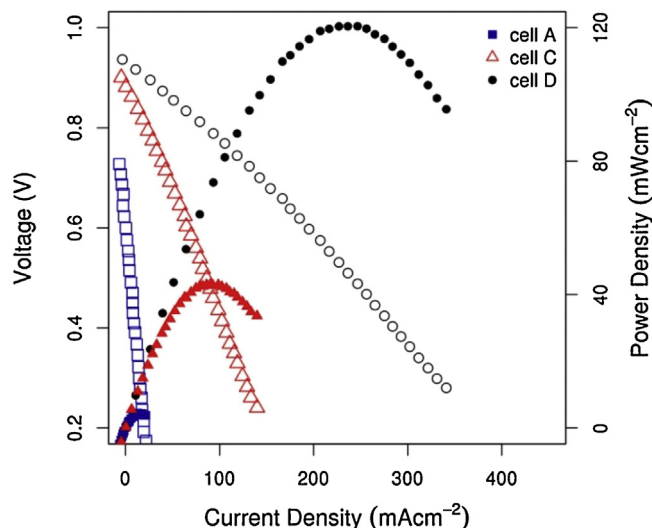


Fig. 2. V-J (open symbols) and power curves (closed symbols) in dry hydrogen at 873 K of (square) cell A, (triangle) cell C, (circle) cell D. Reproducibility tests confirm the behaviour even if absolute values may change ($\pm 10\%$) with respect to those reported here, due to an intrinsic variability in the cell manufacturing.

to ceria alone (cell A). The effect is likely due to an increase in electronic conductivity owing to the presence of a metallic conductor. In our operating conditions tin oxide is likely reduced to Sn^0 ; this observation was confirmed with a post-mortem analysis of the cells. Visual examination of cell B after testing revealed a grey spot at the centre of the anode (see ESI, Fig. S3-A); this showed that tin oxides had been reduced to metallic tin which, in turn, had coalesced and segregated to the surface of the anode. This behaviour is not surprising in light of the strongly reducing environment and the low melting point of tin. It is significant, on the other hand, that when ceria is present tin segregation was not observed (Fig. S3-C, in ESI).

The lowest impedance was reached for cells containing both ceria and tin. Cell D generated the lowest polarization resistance and a well defined EIS spectrum with two clear semicircles. A lower amount of tin (cell C) gave rise to a more complex impedance spectrum with a higher number of RC elements and a higher overall impedance. Increasing the tin content below a Ce:Sn ratio of 1 did not improve performance further (results not shown). These results are in line with a situation in which a Ce:Sn ratio closer to 1 would maximize the area of ceria-tin boundary regions, that is the triple phase boundary (TPB). If considerably less tin is present, it is likely that a higher degree of heterogeneity is present in the anode, which comprises ceria-tin interaction areas and areas where ceria exists alone. Nyquist plots show also that the co-presence of ceria and tin causes a decrease in the contribution at low frequency ($<10 \text{ Hz}$). A lower low frequency capacitance could mean that either the charge transfer, oxygen transfer or the hydrogen adsorption are improved [47]. In all cases, an important contribution to the increase in cell performance is due to tin participating in the oxidation reaction, either through direct interaction with H_2 or through the formation of a reactive triple phase boundary (TPB).

The lower impedance registered when tin is added in an anode infiltrated with ceria naturally translates in an increase in the current and power output of the fuel cell (Fig. 2). The improvement is of a factor of 10 for a Ce:Sn ratio close to 1 (cell D), which reaches a maximum of 120 mW cm^{-2} , and of a factor of approximately 4 for cell C when compared to cell A. The current drawn from cell B, due to the previously mentioned segregation, is extremely low and unstable with a maximum power under 20 mW cm^{-2} (not shown).

Table 2

Atomic percentages obtained from EDX spectra on cell D and cell B. Data were recorded both on particles and on feature-less regions of the SDC scaffold. SEM images and EDX spectra for cell B are available in the Supporting Information.

Cell type	Element	Atomic%	
		On particles	On scaffold
Cell B	O	62.3	63.5
	Sn	1.8	3.6
	Ce	18.0	23.4
	Sm	4.0	5.1
Cell D	O	74.3	67.2
	Sn	13.7	0.8
	Ce	8.7	24.2
	Sm	1.4	5.5

An analysis of the open circuit voltage (OCV) values also support an active role of tin in the oxidation of hydrogen. The OCV increases from 0.8 V for cell A to 0.92 V for cell D, while for tin alone (cell B) the OCV is considerably lower at 0.76 V; in all cases the results were reproducible and stable over a time span of 24 h. For all cells, the OCV is lower than the theoretical value. This can be attributed to an interplay of gas transport limitations caused by the low and imperfect porosity of the anode [48] as well as to its high thickness and to losses deriving from leakage currents through the SDC electrolyte [49]; these factors affect all cells in equal measure. The fact that the presence of tin and ceria together increases the OCV with respect to the separate materials is attributable to reduced activation losses: these include improved mixed ionic and electronic conduction, as well as lower barrier for the oxidation reaction.

3.2. Structural and morphological characterization of the tin-ceria system

To explain the increase in performance registered when ceria and tin are both present in SOFC anodes, as well as the stabilization of tin against segregation, scanning electron microscopy (SEM) and energy dispersive X-ray measurements (EDX) experiments were performed on fuel cells after testing in hydrogen (Fig. 3). SEM images show that ceria is present in the anode in the form of 200–300 nm nanoparticles. Table 2 reports the local atomic percentages obtained from EDX micro analysis, which indicate that these particles are composed of both tin and ceria with a negligible presence of samaria, confirming that they are a result of the infiltration of ceria rather than part of the SDC scaffold. Negligible amounts of tin were detected in the regions between the particles where only the signals of ceria and samaria in a roughly 1:4 ratio were registered. This indicates that tin is localized on the infiltrated ceria and does not cover the SDC scaffold, highlighting a strong metal support interaction between the two materials that allows the stabilization of tin in reducing conditions. In cell B, the EDX analysis was made on flat and corrugated zones (see ESI, Figs. S4 and S5), obtaining a similar Ce/Sm atomic ratio and a comparable amount of tin for the two regions. This suggests that the small corrugations are attributable to morphological defects of the support and that tin is well dispersed on the support when impregnated alone.

The nature of the interaction responsible for the stabilization of tin on ceria was investigated by high resolution transmission electron microscopy performed on ceria powders impregnated with tin oxide. The powders were investigated as prepared and after treatment in dry hydrogen at 873 K to simulate the conditions present in the SOFC anode. HR-TEM images in Fig. 4 show that, for powders not exposed to hydrogen, tin is mostly present as tin oxide nanoparticles (5–10 nm) covering ceria particles (10–15 nm). Spots at 3.1 Å and 2.7 Å in the FT image are ascribed to (1 1 1) and (2 0 0)

crystallographic planes of CeO₂, respectively. The spots at 3.3 Å correspond to the (1 1 0) crystallographic planes of SnO₂.

After reduction in pure hydrogen for 6 h the material consists of crystallites about 10–15 nm in size. These crystallites are mainly CeO₂ and metallic Sn, but there are also SnO_x crystallites. In the inset in Fig. 4D, the Fourier Transform (FT) image shows the pattern of CeO₂ oriented along the (1 1 0) crystallographic direction (spots at 3.1 Å and 2.8 Å corresponding to (1 1 1) and (2 0 0) planes, respectively) and spots at 2.4 Å that are ascribed to (0 0 2) crystallographic planes of SnO. Over all the Sn and SnO crystallites there is a thin layer of amorphous tin oxide about 2–4 nm thick. Most of the ceria crystallites are not covered by this amorphous layer, suggesting that its occurrence is related to tin. Therefore, after strong reduction (6 h) tin is not completely reduced as a few crystallites of SnO_x are present and, more importantly, there is an amorphous layer of tin oxide covering the metallic Sn nano-crystals. The fact that SEM images of fuel cell anodes after testing show that tin is localized on ceria particles suggests that this structure is also present during SOFC operation.

To confirm that the tin oxide shell was a result of the metal-support interaction, the reduction process was also followed by in-house X-ray photoelectron spectroscopy (XPS). Oxidized samples were exposed to hydrogen and analyzed by XPS without being exposed to air in between. Fig. 5 shows the evolution of tin 3d peaks before and after reduction in hydrogen. After treatment in 5% hydrogen the peaks in the Sn 3d XPS spectrum of the as-prepared sample turn into two doublets with the formation of a shoulder at lower binding energy. After further treatment in pure hydrogen the shoulders grow to two absorption peaks at energies characteristic of metallic tin. For both doublets, the contributions related to tin oxide shift to lower binding energies, indicating a reduction of SnO₂ to lower valent tin oxides [50,51]. The results are in line with those obtained with HR-TEM.

The reduction process on ceria powders impregnated with tin oxide was also followed in-situ at 873 K through X-ray diffraction analysis (Fig. 6). It can be seen how the diffraction peaks related to SnO₂ disappear after exposure to hydrogen at 873 K. After the temperature is lowered to room temperature the diffraction peaks of metallic tin appear in the spectrum. The peaks belonging to metallic tin then disappear when the temperature is raised above the melting point of Sn⁰ and reappear when the temperature is lowered again; this process is reversible over multiple cycles, showing that tin nanoparticles are composed of molten Sn⁰ operating at intermediate temperature conditions.

The thin oxide shell covering tin nanoparticles was not visible in the spectra, despite being clearly detected by both XPS and HR-TEM. This can be explained by the tin oxide film being amorphous, as indicated by the HR-TEM analysis, as well as by the very low thickness of the film.

3.3. Mechanism of nanoparticle formation

HR-TEM and XPS data indicate that an initially uniform oxide film is reduced and spontaneously re-organizes to form core-shell like Sn@SnO_x nanoparticles. A mechanism to explain this transition is proposed in Fig. 7. XRD and XPS spectra show that tin oxide is gradually reduced to metal upon exposure to hydrogen (steps 1 and 2); as metallic tin begins to form, it melts due to the temperature being considerably higher than that of the melting point of the metal. The molten metal then naturally starts to coalesce into droplets (step 3); the presence of the ceria support, however, allows for a continuous transfer of oxygen atoms from the substrate to the molten metal. The oxygen transfer slows down the reduction process, allowing for the formation of nanometric molten tin droplets, which are stabilized in a dynamic equilibrium in which

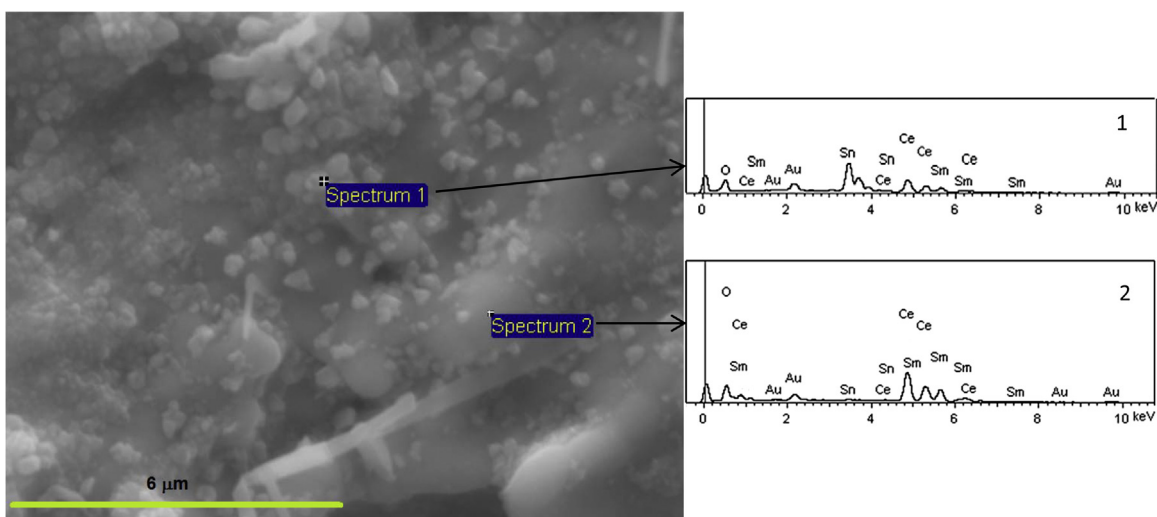


Fig. 3. SEM image of cell D showing 200–300 nm nanoparticles on the SDC anodic scaffold. EDX spectra taken (1) on particles and (2) on the SDC scaffold away from the particles with elemental analysis of Ce, Sm, O, Sn, Au are also presented. Au is present as a consequence of the metallization of the sample.

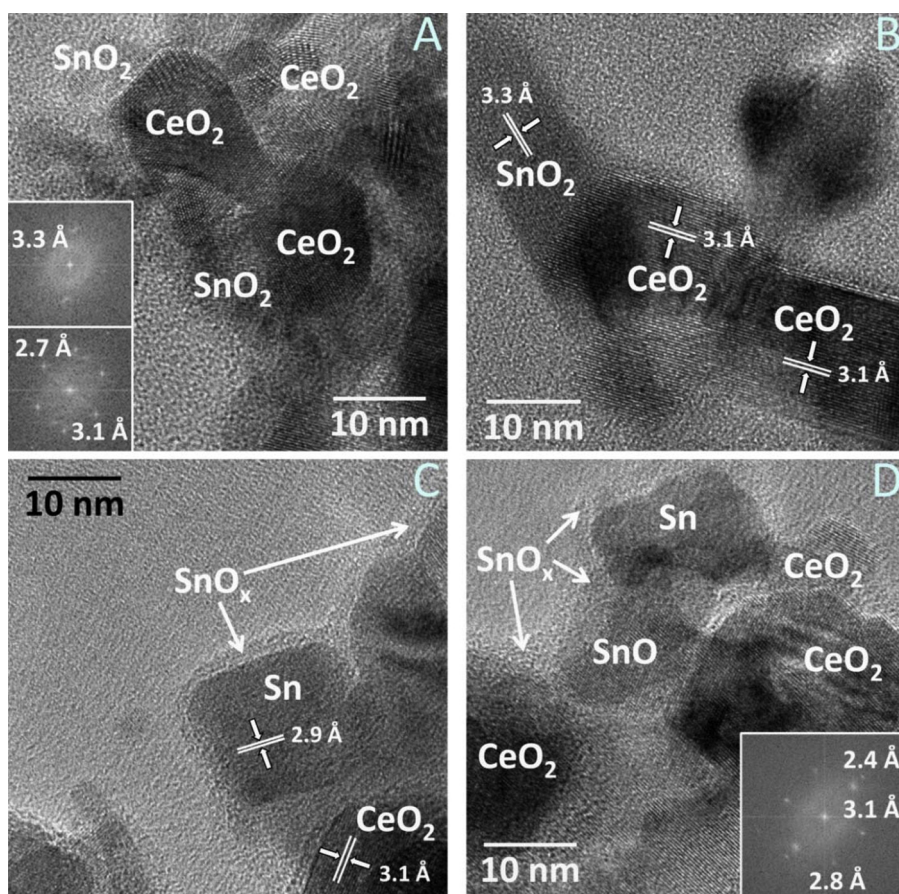


Fig. 4. HR-TEM images of a ceria powder infiltrated with tin oxide (A,B) before and (C,D) after exposure to H_2 at 873 K for 6 h.

tin oxide formation is counterbalanced by reduction to metal. Previous studies suggest that a partial reduction of ceria due to the formation of interfacial Sn^+ species is responsible for an increase of oxygen mobility and consequently for an increase in catalytic activity of Ce–Sn mixed oxides [21]. In this scenario electrons could originate both from Sn^+ or from Sn^0 and the higher reactivity could be related to an improvement of both the electronic and ionic conductivity of CeO_2 . A similar charge-transfer mediated by tin has also

been observed in the case of CO oxidation by platinum–tin catalysts [52] and it has been recently reported as a key mechanism of the metal–ceria interaction [53]. However, in the present case HR-TEM data clearly show that a non-stoichiometric amorphous oxide of tin is present at the triple phase boundary. Even without invoking the formation of Sn^+ species, such a sub-oxide would be able to lower the surface-oxygen bond strength with respect to both ceria and crystalline tin oxide [54,55]. Consequently, the energy

barrier for surface oxygen exchange, which has been described as a bottleneck for the catalytic activity of ceria [56], would also be lowered [20], explaining the increase in electro-catalytic activity registered in fuel cells. Since the SnO_x shell exists in a delicate balance between the oxidative action of the support and the reductive action of the fuel, doubts could arise regarding the longer term stability of the Sn@SnO_x system. Preliminary data obtained via XPS, however, show that exposing ceria-tin samples previously reduced in dry hydrogen to humidified hydrogen generates a significant increase in the intensity of oxidized tin species in Sn 3d spectra (Fig. 8, ratios between oxidized and metallic tin obtained via XPS are available in Table S1 of ESI.). This difference can be ascribed to a thickening of the oxide layer covering Sn^0 nanoparticles after the treatment. Given the shift towards higher binding energy of the peaks corresponding to oxidized tin, it can also be stated that such thickening might involve $\text{Sn(II)} \rightarrow \text{Sn(IV)}$ and/or $\text{Sn(II)} \rightarrow \text{Sn(IV)}$ processes. In a fuel cell, where water is the product of hydrogen oxidation and can also be added to the gas feed, this process could effectively contribute to the long term stabilization of the system. In our study, we did not observe significant changes in the EIS or in the power responses by adding 3% water to the gas feed. This does not exclude an influence of water on the stabilization of the

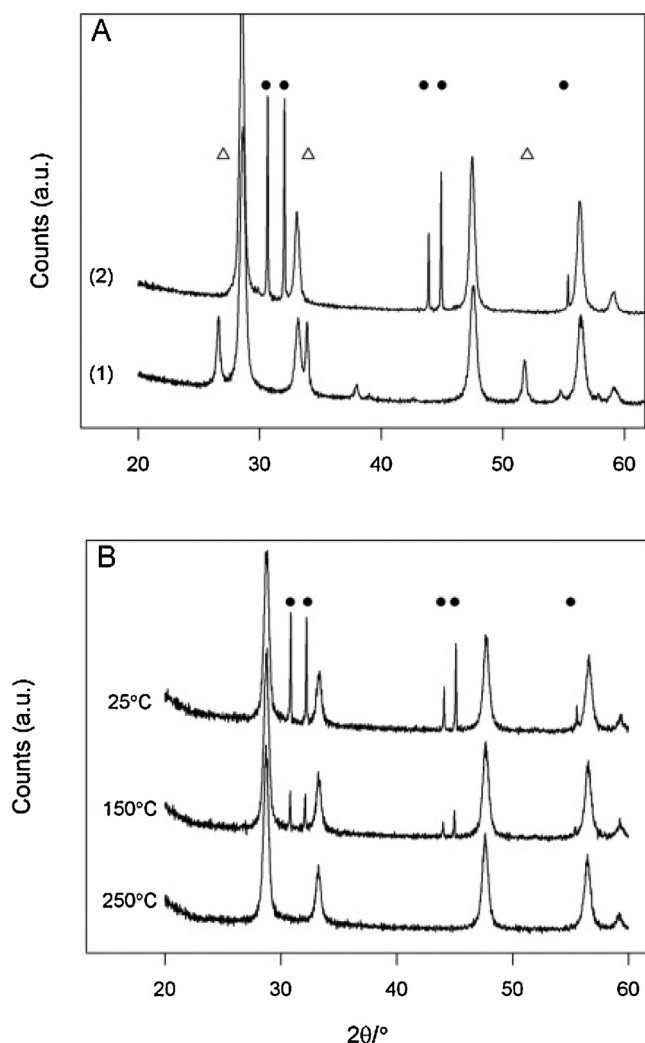


Fig. 6. (A) XRD spectra of ceria-tin oxide powders before (spectrum 1) and after (spectrum 2) treatment at 873 K with hydrogen for 3 h. Dots mark diffraction peaks of metallic tin, triangles those of tin oxide. (B) XRD spectra of reduced ceria-tin powders at different temperatures above and below the melting point of metallic tin. Dots mark the diffraction peaks of metallic tin.

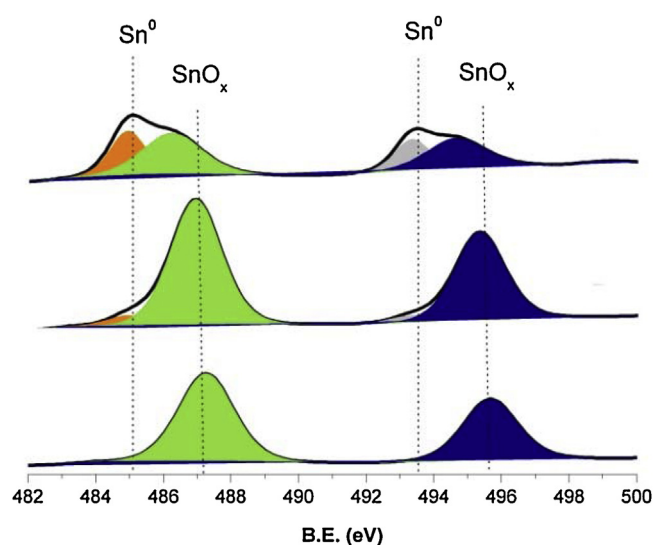


Fig. 5. Sn 3d XPS spectra. From bottom to top spectra were recorded on (1) as prepared SDC pellets infiltrated with ceria and tin oxide, (2) after reductive treatment at 873 K in 5% H_2 in Ar and (3) after a second reductive treatment at 873 K in pure H_2 .

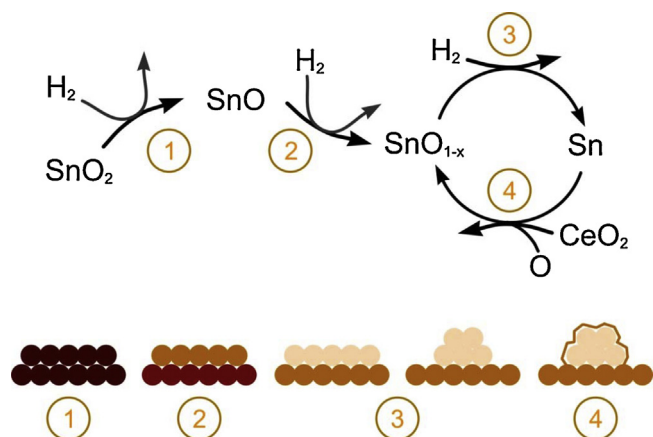


Fig. 7. Proposed mechanism for the formation and stabilization of molten Sn@SnO_x nanoparticles. (1) Homogeneous tin(IV) oxide film. (2) Reduction to tin(II) oxide and further reduction to a tin suboxide. (3) Further reduction, formation of molten metallic tin and coalescence of the molten metal. (4) Oxygen transfer from ceria and surface re-oxidation of the molten tin nanoparticles.

tin-ceria system; rather, the effect could not be appreciated through the analysis of macroscopic parameters such as cell impedance and power density. It is pointed out that in the tin-ceria system water has the role to maintain oxidized the surface of tin rather than to favour the mechanism of oxygen transport through the formation of mobile surficial hydroxyl groups as it occurs in other ceria based anodes.

These preliminary results could also mean that a stabilization of the core-shell structures may be possible also in other catalytic applications. Having an oxygen source in the gas phase, in fact, could help stabilize the SnO_x shell surrounding metallic tin even without a steady supply of oxygen atoms from a cathode.

The data discussed so far underline the role of tin/tin oxide as a mediator for oxygen exchange, which could aid in the reduction of ceria and oxygen release. Overall, the study highlights the importance of the triple phase boundary in promoting the formation of catalytically active phases. At the TPB, in fact, the redox interaction between an oxygen-donating support like ceria and a metal can promote the formation of sub-stoichiometric amorphous oxides

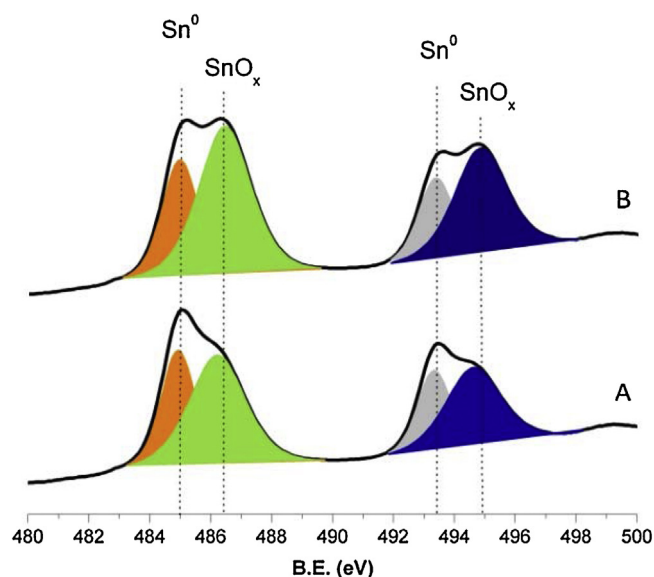


Fig. 8. Sn 3d XPS spectra. Spectra were recorded on as prepared SDC pellets infiltrated with ceria and tin oxide (A) after reductive treatment at 873 K in pure H_2 and (B) after a second reductive treatment at 873 K in H_2 with 3% water.

which can greatly enhance the catalytic properties with respect to both the metal and the support [57]. In this context, augmenting the area of the TPB by appropriately tailoring the size and shape of ceria particles together with the size of the supported metal nanostructures could then allow to maximize electro-catalytic activity [58] by extending the area of such amorphous oxides. Experimental evidence, in fact, suggests that rather than focusing either on the action of the support or of the metal nanostructures, the attention should be directed to promoting their redox interaction in order to create sub-stoichiometric metal-support junctions. In addition, the presence of a molten metal could effectively augment the contact area between the metal nanostructures and the support, thereby further promoting their interaction.

The $Sn@SnO_x/CeO_2$ structures described in this work could then serve as a new model for the development of metal-support systems in which both the metal and the metal oxide support contribute to the formation and stabilization of an amorphous low-valent MO_x interface, more reactive than the corresponding MO_x crystalline oxide [59].

4. Conclusions

Samaria-doped ceria anodes infiltrated with ceria and tin oxide were tested at intermediate temperature with dry hydrogen as the fuel. It was found that the presence of tin in ceria infiltrated SOFC anodes enhances the catalytic properties of ceria towards the oxidation of hydrogen at 873 K, causing a 10-fold increase in power output. XRD analysis of ceria powders impregnated with tin oxide show that, upon exposure to hydrogen at 873 K, SnO_2 is reduced to molten metallic tin. XPS and HR-TEM experiments revealed that the molten tin is stabilized in molten metal core-shell nanostructures on ceria particles at temperatures up to 400 °C, above its melting point. The fundamental role of ceria in the process of stabilization and promotion of these nano-structures has been highlighted. The stabilization is possible thanks to a transfer of oxygen from ceria to the tin nanoparticles and the formation of an amorphous oxide on their surface, which help avoid coalescence of the nanoparticles. It is likely that the amorphous nature of the SnO_x shell can be responsible for the improved electro-catalytic activity registered thanks to a weakened surface-oxygen bond with respect to both ceria and

crystalline tin oxide. These findings highlight that metal oxides supported on ceria under controlled reducing conditions may give rise to a self-assembly of more reactive surfaces when the temperature is risen above the melting point of the catalyst. This could constitute a novel example for synthetic routes towards multi-functional catalysts and active heterostructures.

Acknowledgments

The authors would like to thank Dr. G. Gregori at the Max Planck Institut für Festkörperforschung for helpful discussion. Funding from the Italian Ministry of University and Research (MIUR) for the BIO-ITSOFC project (2010KHLKFC 003, PRIN 2010–2011) and MINECO project ENE201236368 is gratefully acknowledged. J. Llorca is a Serra Hunter Fellow and is grateful to the ICREA Academia program.

Appendix A. Supplementary data

Supplementary data associated with this article can be found, in the online version, at <http://dx.doi.org/10.1016/j.apcatb.2016.02.050>.

References

- [1] A. Trovarelli, Catal. Rev. 38 (1996) 438–520.
- [2] M. Batzill, U. Diebold, Prog. Surf. Sci. 79 (2005) 47–154.
- [3] A. Trovarelli, P. Fornasiero, Catalysis by Ceria and Related Materials, Imperial College Press, London, 2013.
- [4] A. Trovarelli, C. de Leitenburg, M. Boaro, G. Dolcetti, Catal. Today 50 (1999) 353–367.
- [5] W. Lu, L. Worrell, J.M. Vohs, R.J. Gorte, J. Electrochem. Soc. 150 (2003) A1357–A1359.
- [6] W. Sun, W. Liu, J. Power Sources 217 (2012) 114–119.
- [7] A. Katsuki, K. Fukui, Sens. Actuators 52 (1998) 30–37.
- [8] M.M. Gadgil, R. Sasikala, S.K. Kulshreshtha, J. Mol. Catal. 87 (1994) 297–309.
- [9] N. Oka, S. Yamada, T. Yagi, N. Taketoshi, J. Jia, Y. Shigesato, J. Mater. Res. 29 (2014) 1579–1584.
- [10] S. Mihaiu, L. Marta, M. Zaharescu, J. Eur. Ceram. Soc. 27 (2007) 551–555.
- [11] T. Nguyen, J. Deloume, V. Perrichon, Appl. Catal. A: Gen. 249 (2003) 273–284.
- [12] A. Gambhire, M.K. Lande, S. Kalokhe, M. Shirsat, K. Patil, R. Gholap, B. Arbad, Mater. Chem. Phys. 112 (2008) 719–722.
- [13] R. Sasikala, N. Gupta, S. Kulshreshtha, Catal. Lett. 71 (2001) 69–73.
- [14] A. Vasile, V. Bratan, C. Hornoio, M. Caldararu, N. Ionescu, T. Yuzhakova, A. Redey, Appl. Catal. B 140–141 (2013) 25–31.
- [15] S. Somacescu, R. Scurtu, G. Epurescu, R. Pascu, B. Mitu, P. Osiceanu, M. Dinescu, Appl. Surf. Sci. 278 (2013) 146–152.
- [16] T. Baidya, A. Gupta, P. Deshpandey, G. Madras, M. Hegde, J. Phys. Chem. C 113 (2009) 4059–4068.
- [17] A. Maciel, P. Lisboa-Filho, E. Leite, C. Paiva-Santos, W. Schreiner, Y. Maniette, E. Longo, J. Eur. Ceram. Soc. 23 (2003) 707–713.
- [18] X. Xu, R. Zhang, X. Zeng, X. Han, Y. Li, Y. Liu, X. Wang, ChemCatChem. 5 (2013) 2025–2036.
- [19] X. Zeng, R. Zhang, X. Xu, X. Wang, J. Rare Earths 30 (2012) 2013–2019.
- [20] Y. Zhao, B. Teng, Z. Yang, Y. Zhao, L. Zhao, M. Luo, J. Phys. Chem. C 115 (2011) 16461–16466.
- [21] V. Matolín, M. Cabala, V. Cháb, I. Matolínová, K.C. Prince, M. Škoda, F. Šutara, T. Scála, K. Veltruská, Surf. Interface Anal. 40 (2008) 225–230.
- [22] M. Škoda, M. Cabala, V. Cháb, K. Prince, L. Sedláček, T. Skála, F. Šutara, V. Matolín, Appl. Surf. Sci. 254 (2008) 4375–4379.
- [23] T. Skála, F. Šutara, K. Prince, V. Matolín, J. Elect. Spect. Phen. 169 (2009) 20–25.
- [24] R. Vidu, C. Placianu, C. Bartha, Ind. Eng. Chem. Res. 53 (2014) 7829–7839.
- [25] E. Aneggi, D. Wiaters, C. de Leitenburg, J. Llorca, A. Trovarelli, ACS Catal. 4 (2014) 172–181.
- [26] M. Melchionna, P. Fornasiero, Mater. Today 17 (2014) 349–357.
- [27] M. Tinoco, S. Fernandez-Garcia, M.B. Lopez-Haro, A. Hungria, X. Chen, G. Blanco, J. Perez-Omil, S. Collins, H. Okuno, J. Calvino, ACS Catal. 5 (2015) 3504–3513.
- [28] T. Desauany, G. Bonura, V. Chiodo, S. Freni, J.-P. Couzinié, J. Bourgon, A. Ringuedé, F. Labat, C. Adamo, M. Cassir, J. Catal. 297 (2013) 193–201.
- [29] V. Solovyov, T. Ozaki, A. Atrei, L. Wu, A. Al-Mahboob, J.T. Sadowski, X. Tong, D. Nykypanchuk, Q. Li, Sci. Rep. 4 (2014).
- [30] M. Zabilskiy, P. Djinić, E. Tchernychova, O.P. Tkachenko, L.M. Kustov, A. Pintar, ACS Catal. 5 (2015) 5357–5365.
- [31] L. Kundakovic, M. Flytzani-Stephanopoulos, J. Catal. 179 (1998) 203–221.
- [32] C.M.Y. Yeung, K.M.K. Yu, Q.J. Fu, D. Thompson, M.I. Petch, S.C. Tsang, J. Am. Chem. Soc. 127 (2005) 18010–18011.
- [33] Q. Fu, H. Saltsburg, M. Flytzani-Stephanopoulos, Science 301 (2003) 935–938.
- [34] J.A. Farmer, C.T. Campbell, Science 329 (2010) 933–936.

- [35] A. Longo, L.F. Liotta, G. Pantaleo, F. Giannici, A.M. Venezia, A. Martorana, J. Phys. Chem. C 116 (2012) 2960–2966.
- [36] G. Zafiris, R. Gorte, J. Catal. 139 (1993) 561–567.
- [37] J. Xu, S. Overbury, J. Catal. 222 (2004) 167–173.
- [38] H. Cordatos, T. Bunluesin, J. Stubenrauch, J.M. Vohs, R. Gorte, J. Phys. Chem. 100 (1996) 785–789.
- [39] S. Colussi, F. Amoroso, L. Katta, J. Llorca, A. Trovarelli, Catal. Lett. 144 (2014) 1023–1030.
- [40] H. Kan, S.H. Hyun, Y.-G. Shul, H. Lee, Catal. Comm. 11 (2009) 180–183.
- [41] A. Singh, J. M. M.J. Hill, Power Sources 214 (2012) 185–194.
- [42] H. Kan, H. Lee, Appl. Catal. B: Environ. 97 (2010) 108–114.
- [43] H. Abernathy, R. Gemmen, K. Gerdes, M. Koslowske, T. Tao, J. Power Sources 196 (2011) 4564–4572.
- [44] A. Jayakumar, S. Lee, A. Hornes, J. Vohs, R. Gorte, J. Electrochem. Soc. 157 (2010) B365–B369.
- [45] T. Suzuki, Z. Hasan, Y. Funahashi, T. Yamaguchi, Y. Fujishiro, M. Awano, Science 325 (2009) 852–855.
- [46] Y. Lin, C. Su, C. Huang, J.S. Kim, C. Kwak, Z. Shao, J. Power Sources 197 (2012) 57–64.
- [47] Q.-A. Huang, R. Hui, B. Wang, J. Zhang, Electrochim. Acta 52 (2007) 8144–8164.
- [48] H.-S. Noh, H. Lee, B.-K. Kim, H.-W. Lee, J.-H. Lee, J.-W. Son, J. Power Sources 196 (2011) 7169–7174.
- [49] D. Cui, Q. Liu, F. Chen, J. Power Sources 195 (2010) 4160–4167.
- [50] K. Ke, K. Waki, J. Electrochem. Soc. 154 (2007) A207–A212.
- [51] A. Lewera, P.J. Barczuk, K. Skorupska, K. Miecznikowski, M. Salamonczyk, P.J. Kulesza, J. Electroanal. Chem. 662 (2011) 93–99.
- [52] C. Dupont, Y. Jugnet, F. Delbecq, D. Loffreda, J. Catal. 273 (2010) 211–220.
- [53] G.N. Vayssilov, Y. Lykhach, A. Migani, T. Staudt, G.P. Petrova, N. Tsud, T. Skala, A. Bruix, F. Illas, K.C. Prince, V. Matolin, K.M. Neyman, J. Libuda, Nat. Mater. 10 (2011) 310–315.
- [54] M. Scurtu, S. Mihaiu, M. Caldararu, M. Zaharescu, React. Kinet. Mech. Cat. 105 (2012) 135–144.
- [55] C. Yoon, D.L.J. Cocke, Non Cryst. Solids 79 (1986) 217–245.
- [56] C. Chatzichristodoulou, P. Blennow, M. Sogaard, P. Hendriksen, M. Mogensen, Catalysis by Ceria and Related Materials, in: A. Trovarelli, P. Fornasiero (Eds.), Imperial College Press, London, 2013.
- [57] M. Wong, W. Knowles, E. Ross, I. Wachs, ACS Natl. Meet. Book Abstr. 228 (2004), CATL–15.
- [58] M. Cargnello, V.V.T. Doan-Nguyen, T.R. Gordon, R.E. Diaz, E.A. Stach, R.J. Gorte, P. Fornasiero, C.B. Murray, Science 341 (2013) 771–773.
- [59] H. Li, W. Wang, H. Li, J.-F. Deng, J. Catal. 194 (2000) 211–221.